

# Characterization of the terahertz near-field output of parallel-plate waveguides

Hui Zhan, Rajind Mendis, and Daniel M. Mittleman\*

*Electrical and Computer Engineering Department, Rice University, 6100 Main Street, Houston, Texas 77005, USA*

\*Corresponding author: *daniel@rice.edu*

Received November 1, 2010; accepted November 19, 2010;  
posted December 23, 2010 (Doc. ID 137440); published February 28, 2011

We experimentally characterize the field confinement properties of various parallel-plate waveguide (PPWG) geometries in the terahertz spectral range. In contrast to infinite-width PPWGs with free-space diffraction along the unshielded direction, finite-width (and also tapered) PPWGs show well-confined THz fields at the output facet. Both the transverse field component, perpendicular to the inside surfaces, and the longitudinal component, parallel to the propagation direction, exhibit strong lateral confinement. We also observe an antisymmetric longitudinal field distribution across the air gap, analogous to the symmetric surface plasmon polariton mode observed in optical slot waveguides. © 2011 Optical Society of America

OCIS codes: 230.7370, 240.6680.

## 1. INTRODUCTION

The ability to guide and manipulate electromagnetic waves on a subwavelength scale has been a topic of ongoing interest for many decades, especially for applications in high-resolution imaging and localized sensing. One technique that has been exploited for overcoming the diffraction limit relies on tapered waveguides, which have recently received renewed attention due to the underlying concepts of plasmonics. Plasmonic waveguides have been widely studied in the optical and near-infrared regions, showing extreme subwavelength confinement in various types of metallic structures [1–22]. One important class of such guiding structures, called slot waveguides, relies on the excitation of surface plasmon polaritons (SPPs) localized at a metal corner or edge [10–12]. These are of particular interest because the supported long-range SPP mode shows no long-wavelength cutoff limitation even for the smallest slot size [11].

Recent numerical simulations and experimental studies have successfully extended the concept of plasmonic waveguides down to the THz frequency range [23–30]. For example, Klein *et al.* have reported a  $\sim 20\ \mu\text{m}$  spatial resolution by using a  $30\ \mu\text{m} \times 40\ \mu\text{m}$  rectangular-tip metal/dielectric antenna. This antenna has a tapered slot waveguide structure but with a high index silicon slab sandwiched between the metal surfaces to provide better lateral confinement as achieved in a dielectric slab waveguide [24]. A theoretical study by Rusina *et al.* has predicted that the size of the THz spot concentrated by a class of tapered parallel-plate waveguides (PPWGs) is limited to the skin depth ( $\sim 100\ \text{nm}$ ) of the metallic material, in the case of the symmetric SPP mode [26]. Wächter *et al.* showed experimentally that a finite-width PPWG can effectively guide THz waves with both vertical and lateral confinements as small as  $300\ \mu\text{m}$ , approximately equal to the wavelength [25]. Recently, we reported that tapered PPWGs could be used for squeezing THz waves to a subwavelength scale, better than  $\lambda/250$ , in the transverse dimension parallel to the plate surfaces [30].

In this report, we present comprehensive experimental studies of the THz near-field output of PPWGs with different

plate widths and plate separations, both with and without tapering. Our experiments show that the near-field output radiation from a finite-width PPWG has a much narrower beam width than that from an infinite-width PPWG. We also observe that the beam width scales with the tapered plate width. We employ a scattering-probe imaging technique to study the longitudinal electric field component—that is, the field component parallel to the propagation direction. This longitudinal electric field component exhibits strong confinement at the output of the waveguide in both the unshielded direction and the propagation direction. These measurements also indicate that the longitudinal field distribution is antisymmetric, analogous to the symmetric SPP mode in similar structures demonstrated in the optical regime. These tapered waveguides show broadband guiding, with no spectral distortions or cutoff behavior. Our results provide valuable information for understanding the relevance of surface plasmons in the propagation and confinement behavior of THz radiation in metal waveguides.

## 2. INFINITE-WIDTH (IDEAL) PPWG

PPWGs in the THz range have been studied extensively through observations of the far-field output radiation [31,32], but a complete understanding of the propagation and confinement requires near-field measurements. To this end, we first study the near-field output of a very wide PPWG that can be treated as having an effectively infinite width. In our experiments, a width of 10 cm is much larger than either the input or output beam sizes, so that the energy in the propagating mode is never close to the waveguide (plate) edges. We can treat this situation, which is close to the ideal “textbook” description of a PPWG, as a reference for comparison with subsequent studies of finite-width PPWGs.

Figure 1 shows schematics of the experimental geometries used in this work. The metallic plates are fabricated of highly polished aluminum with a propagation length of 25 cm. The guiding surfaces are polished to a finish of  $0.254\ \mu\text{m}$ . Using a typical terahertz time-domain spectroscopy setup based

on fiber-coupled photoconductive antennas [33], we generate a free-space beam of single-cycle pulses containing spectral components from about 0.05 THz to about 1.0 THz. These are focused onto the input facet of the waveguide, symmetrically located with respect to both transverse axes  $x$  and  $y$ , and with a  $1/e$  diameter of 1 cm. The polarization is chosen to be perpendicular to the inside plate surfaces, to excite the TEM mode of the PPWG at the input [31,34]. We measure the time-domain waveforms at the output facet of the waveguide, and map the near-field spatial distribution. The receiver antenna is oriented so as to be sensitive to the vertical ( $y$ ) component of the field ( $E_y$ ). In order to improve the spatial resolution, a 1 mm diameter aperture is placed in front of the receiver, as in Fig. 1(a).

In Figs. 2(a) and 2(b), we show the spatially resolved 2D profiles of the THz electric field (peak-to-peak amplitude) measured at the output facet of the 10 cm wide PPWG with plate separations of  $b = 10$  and 5 mm, respectively. We observe that the radiation diffracts in the direction parallel to the plate surfaces, with the output beam size (parallel to the surfaces) bigger than the input beam waist. Figure 2(c) shows the 1D profiles of the THz field in the  $x$  direction with plate separations of  $b = 10$ , 5, and 2 mm. The 1D profiles remain Gaussian in shape, similar to the input beam profile, even

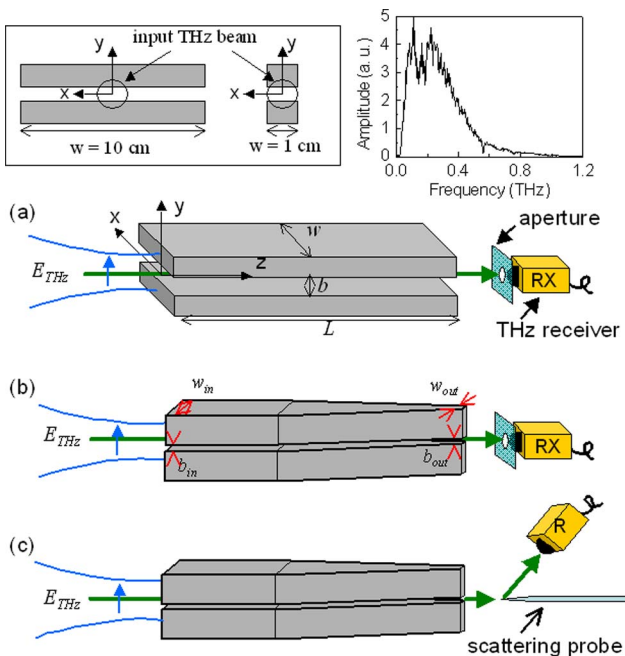


Fig. 1. (Color online) (a) Schematic of the experimental setup showing the THz receiver scanning the output facet of an untapered PPWG. The field is directly detected using a fiber-coupled photoconductive antenna, with an aperture in front of the substrate lens to improve the spatial resolution. The antenna is oriented so as to be sensitive to the  $y$  component of the field. The left inset shows the input coupling configuration for two PPWGs with different widths (10 and 1 cm). The right inset gives a typical spectrum of a detected signal. (b) Schematic for the tapered PPWGs. The input coupling configuration and the THz detection are all kept the same as for the setup in (a), including the aperture. The parameters describing the size of the input and output facet,  $w_{in}$  and  $w_{out}$ , the plate width, and  $b_{in}$  and  $b_{out}$ , the plate separation, are shown. (c) Modified schematic for the tapered PPWGs. In this case, an aperture-based method provides inadequate spatial resolution, so a scattering-probe technique is employed. Here, the measurement is sensitive to the  $z$  component of the electric field. The field can be characterized by scanning the position of the probe.

as the plate separation decreases. Because there is no discontinuity of the waveguide in the  $x$  direction (because the beam remains far from the plate edges), the 1D Gaussian beam diffraction starting from the location of the input facet produces a Gaussian profile along this axis. The full width at half-maximum (FWHM) is about 4.5 cm, which is consistent with the propagation distance of 25 cm for the input focusing conditions used in these measurements and for the peak-amplitude wavelength of the input pulse.

Another interesting observation is that the THz field is not uniformly distributed in the  $y$  direction, as one might expect for a pure TEM mode in a PPWG. The 1D THz field profiles along the vertical ( $y$ ) axis, shown in Fig. 2(d), were measured at the center of the waveguide, indicated by the black dashed lines in Figs. 2(a) and 2(b). At a relatively large plate separation  $b = 10$  mm, the  $y$ -axis profile shows that the THz signals reach local maxima near the metal surfaces, with a central lobe at the center of the guiding area. This THz field is evidently not a pure TEM mode, because the fundamental TEM mode should exhibit no spatial dependence along the  $y$  axis.

This enhancement near the surfaces could be explained as a hybrid mode, composed of a superposition of a TEM-like mode combined with surface plasmon waves bound to the surfaces of the upper and lower metal plates. Such hybrid modes have been discussed previously in the context of microwave waveguides [35–37], but to our knowledge they have not previously been experimentally observed in the THz regime. Of course, the ideal TEM mode, with a uniform spatial profile along the  $y$  axis, only exists in the case of perfect electric conductors with infinite conductivity. When the metal conductivity is finite, such that surface plasmons can be supported, one may expect such a hybrid mode, especially in the case where the plate separation is larger than the characteristic length for the plasmon decay into the air. Indeed, it has previously been shown, by far-field THz measurements, that the gradual separation of the two metal plates of a PPWG gives rise to bound surface waves, i.e., SPPs, on the two separate surfaces [38]. In our case, where the plate separation is fixed ( $b = 10$  mm) but comparable to the experimentally estimated value of the plasmon decay length into air of 7.6 mm, a hybrid mode can be formed because the phase velocity of the TEM mode and of the surface plasmon mode are essentially equivalent, both equal to the speed of light in air to within a few parts in  $10^8$  [38,39]. Because surface plasmon waves are relatively loosely bound to the metal surface in the THz range, compared to those at optical frequencies, these THz surface plasmon waves can be distinguished by making a spatially resolved near-field measurement at the output facet of the waveguide, when the plates are well separated. We note that a far-field measurement would not be able to distinguish a propagating TEM mode from a surface plasmon mode or a hybrid mode. Thus, the near-field measurements reported here are necessary to characterize this behavior.

Figure 2(d) also shows the profile from an infinite-width PPWG with a smaller plate separation  $b = 5$  mm. We observe a more uniform spatial distribution of the THz electric field along the  $y$  direction, closer to an ideal TEM mode. This indicates that when the plate separation decreases, the exponential tails of the two surface plasmon waves from the two metal plates overlap more strongly within the air gap, and the distinction between them becomes much less clear.

This contrasts to the case of a large plate separation, where the spatial decay of the surface plasmon is observed more clearly.

### 3. FINITE-WIDTH PPWG

With this understanding of the THz output mode in the infinite-width PPWG, we now turn to the case of a finite plate width, studied with the same experimental setup. In this case, the 1 cm plate width matches the input THz beam size, as shown in the inset of Fig. 1(a). Similar to Figs. 2(a) and 2(b), the 2D output profiles, measured with a plate separation of  $b = 10$  and 5 mm, are shown in Figs. 3(a) and 3(b), respectively. In contrast to the diffracted field seen in the infinite-width PPWG (Fig. 2), these field maps from the narrower PPWGs show that the output THz field is confined to a region only slightly larger than the width of the waveguide, even along the unshielded ( $x$ ) direction. Figure 3(c) shows cuts of the 1D field profiles along  $x$  for several different plate separations ( $b = 10, 5,$  and 2 mm), as indicated by the white horizontal dashed lines in Figs. 3(a) and 3(b). Unlike in the case of the infinite-width PPWG, these field profiles depend strongly on the plate separation. The departure from a Gaussian profile becomes more pronounced as the plate separation decreases. We also observe field enhancement near the four sharp corners of the metal plates, more clearly presented in Fig. 3(d). These 1D profiles were measured along the two vertical black dotted lines in Fig. 3(a). The field near the corners is  $\sim 35\%$  larger than that near the flat plate surfaces at  $x = 0$ . This field enhancement appears to be evidence for plasmonic edge mode formation [10–12], propagating along the sharp corners of the metal plates. It has been suggested that such edge modes can couple to each other across the air gap between the plates, providing a mechanism for plasmon-mediated energy confinement in optical slot waveguides [14]. This suggested confinement mechanism, relevant in the near-infrared regime, also appears to be important at THz frequencies.

To characterize the degree of energy confinement inside the finite-width PPWG, we define an energy confinement factor, given by the ratio of the energy within the waveguide (in the rectangular region between the plates) to the total energy reaching the output plane (i.e., the plane of the waveguide output facet). Figure 4 shows this confinement factor as a function of the plate separation with the 1 cm wide waveguide, extracted directly from our measurements. The insets schematically illustrate the definition of the confinement factor indicating the relevant cross-sectional areas. These data fit well to an exponential dependence, converging to unity at a zero plate separation [30]. This result supports the possibility of achieving very high energy confinement in extremely narrow PPWGs.

### 4. TAPERED PPWGs

We now turn to the case of tapered PPWGs, which can provide a route to subwavelength field confinement. We studied several different waveguides with various geometrical parameters, as listed in Table 1. Each metal plate has an input width  $w_{\text{in}} = 1$  cm and tapers uniformly down to an output width  $w_{\text{out}}$ , after an untapered input section. The length of the untapered part is 5 cm (in all the waveguides), and the length of the tapered part is either 5 or 20 cm. In these measurements, the plate separation  $b$  is also varied. Because the

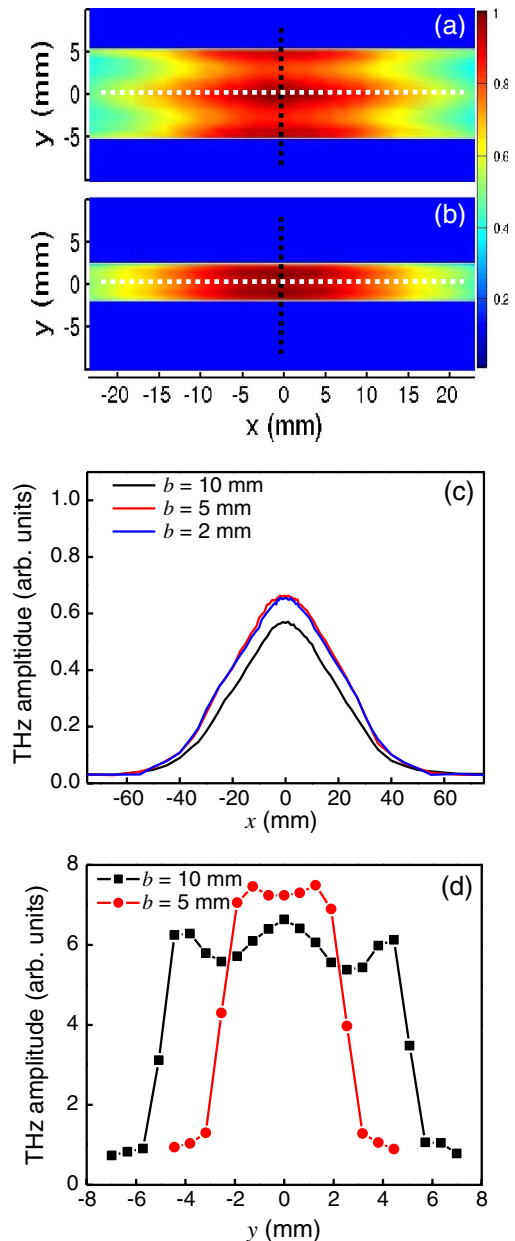


Fig. 2. (Color online) Two-dimensional profiles of the THz electric field (peak-to-peak amplitude) measured at the output facet of the 10 cm wide PPWG with a plate separation (a)  $b = 10$  and (b) 5 mm. (c) One-dimensional  $x$ -axis scans for the 10 cm wide PPWG for three different plate separations,  $b = 10, 5,$  and 2 mm. (d) Vertical profiles of the field along the black dashed lines in (a) and (b) showing the non-uniform profiles along the  $y$  direction.

vertical confinement provided by the metal plate boundary is easy to understand, we first keep the plates parallel to each other ( $b = b_{\text{in}} = b_{\text{out}}$ ) to focus our studies on the lateral confinement behavior due to the tapered plate width.

In these measurements, we use the same experimental setup as described above, for detecting the transverse field component  $E_y$ , shown in Fig. 1(b). As before, the spatial resolution is limited by the 1 mm diameter aperture in front of the receiver. We first map  $E_y$  along the  $x$  axis at the end of 10 cm long waveguides (S1–S4) with different output widths at a plate separation of  $b = 1$  mm. These results are shown in Fig. 5(a). In Fig. 5(b), we show the FWHM of the output spot as a function

of the output width, for different plate separations. Clearly, when the plate separation is large, the output spot size does not change with the width. This is consistent with our understanding of the confinement mechanism, which relies on the mutual coupling of edge plasmons. For large plate separation, this coupling is weak, so the dependence on plate width is also weak. When the plate separation is reduced, the coupling of edge plasmons across the air gap becomes stronger and the radiation spot changes roughly in proportion with the width.

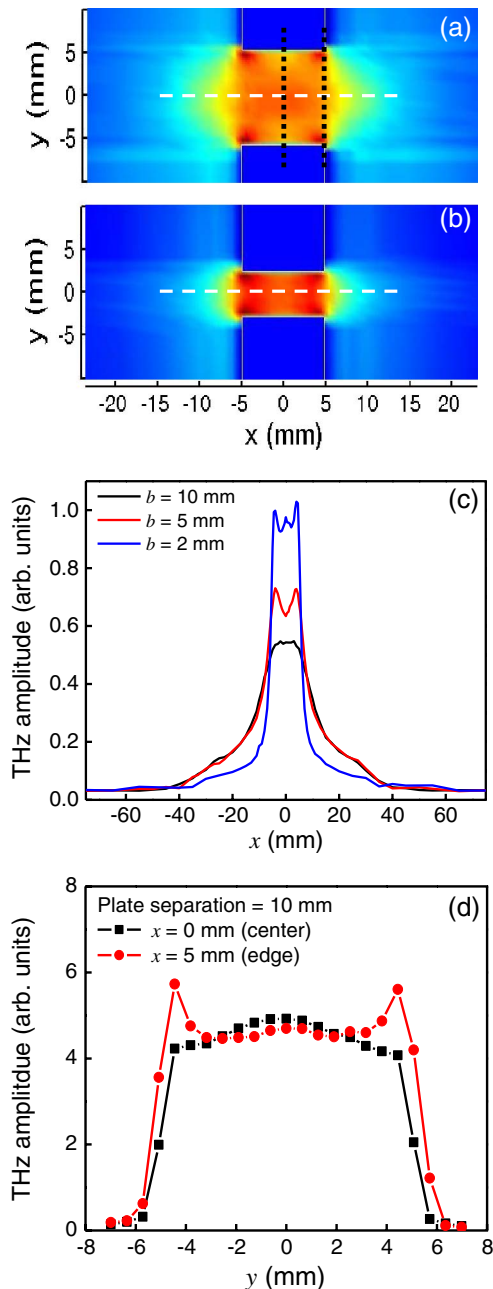


Fig. 3. (Color online) Two-dimensional profiles of the THz electric field (peak-to-peak amplitude) measured at the output facet of the 1 cm wide PPWG with a plate separation of (a)  $b = 10$  and (b) 5 mm. Here, the edge plasmons are clearly observed at the four corners corresponding to the two metal plates. (c) One-dimensional  $x$ -axis scans for the 1 cm wide PPWG for three different plate separations,  $b = 10$ , 5, and 2 mm. (d) Vertical profiles along the black dashed lines in (a), showing the field enhancement near the corners, which do not appear at the center.

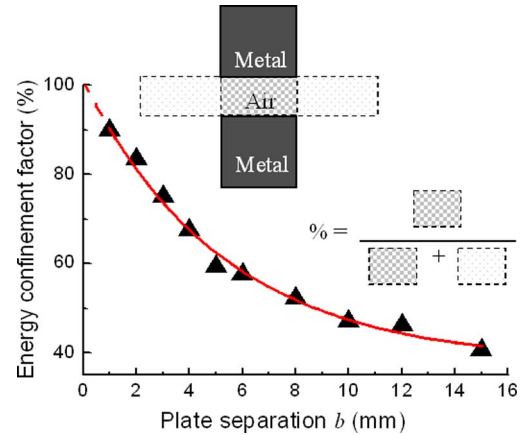


Fig. 4. (Color online) Energy confinement factor as a function of the plate separation. The insets schematically illustrate how this confinement factor is defined. The curve is a fit to an exponential dependence, converging to unity at a zero plate separation.

However, for  $b = 2$  mm, we note that the FWHM of the THz beam from the waveguide S4 with  $w_{\text{out}} = 0.2$  mm is even bigger than S2 with  $w_{\text{out}} = 1$  mm and S3 with  $w_{\text{out}} = 2$  mm. In the case of waveguide S4, the output width ( $w_{\text{out}} = 0.2$  mm) is much smaller than the plate separation ( $b = 2$  mm). This could indicate a more complex mutual coupling of the four edge plasmons, which may result in less efficient field confinement.

Next, we perform the same measurements on the 25 cm long waveguides (L1–L4), and these results are shown in Fig. 6. Comparing with the results from the shorter waveguides, we note that the FWHM corresponding to the outputs from the long waveguides (with more gradual tapering) are generally always smaller than those from the short waveguides. For waveguides L3 and L4 with  $w_{\text{out}} = 1$  mm and 0.2 mm, with  $b = 1$  mm, the amplitudes of the THz field at the center of the long waveguides ( $x = 0$  mm) are larger than those of the short waveguides (S3 and S4). This indicates that waveguides with longer taper lengths (smaller taper angles) provide better lateral confinement. The better confinement efficiency overcomes the predictably higher overall ohmic loss in the longer waveguides. We also note that when the plate separation is small, the local edge enhancements corresponding to the edge plasmons are only observed in the waveguide S1 with the 10 cm length, shown as the black line in Fig. 5(a). For the other cases, the THz electric fields exhibit a single maximum at the waveguide center. A possible explanation is that when the plates are narrow enough and close enough together, the mutual coupling of the edge plasmons inside such small guiding areas is so strong that the local edge enhancements near the corners are limited in both magnitude and size, and are too small to be detected with our limited spatial resolution. Similar results have been seen in previous numerical simulations [40,41].

Based on these results, we understand that in order to successfully focus THz radiation along a tapered PPWG to a subwavelength spot, both the plate width and separation should taper adiabatically, with the plate separation matching the plate width at the output. Then the THz radiation at the end of a tapered PPWG can be squeezed down to the area which is only determined by the  $x$  and  $y$  dimensions of the output facet (as long as they are bigger than the skin depth in the metal [26]). We can now explore the possibility of subwavelength-scale confinement in both spatial dimensions

**Table 1. Geometric Parameters of the Tapered PPWGs**

Waveguide	Input Width $w_{in}$	Output Width $w_{out}$	Untapered Length	Tapered Length	Total Length
S1	1 cm	5 mm	5 cm	5 cm	10 cm
S2	1 cm	2 mm	5 cm	5 cm	10 cm
S3	1 cm	1 mm	5 cm	5 cm	10 cm
S4	1 cm	0.2 mm	5 cm	5 cm	10 cm
L1	1 cm	5 mm	5 cm	20 cm	25 cm
L2	1 cm	2 mm	5 cm	20 cm	25 cm
L3	1 cm	1 mm	5 cm	20 cm	25 cm
L4	1 cm	0.2 mm	5 cm	20 cm	25 cm
M1	1 cm	120 $\mu\text{m}$	5 cm	20 cm	25 cm
M2	1 cm	100 $\mu\text{m}$	5 cm	20 cm	25 cm
M3	1 cm	40 $\mu\text{m}$	5 cm	20 cm	25 cm
M4	1 cm	10 $\mu\text{m}$	5 cm	20 cm	25 cm

using a PPWG with tapers that satisfy these requirements. Here, we use a tapered PPWG (waveguide M1) 25 cm long, of which the last 20 cm tapers uniformly from an initial width of 10 mm down to a final width of  $\sim 120 \mu\text{m}$  ( $\theta_{\text{taper}} \sim 3^\circ$ ). The plate separation also decreases uniformly from 1 mm (at the input end) down to  $100 \mu\text{m}$ . To characterize the field distribution at the output, we replace the 1 mm aperture with a  $200 \mu\text{m}$  aperture, which still permits the detection of a THz pulse with a reasonable signal-to-noise ratio. This aperture is held about  $200 \mu\text{m}$  away from the output facet, and, therefore, the spatial distribution is broadened due to both free-space diffraction and convolution with the aperture. Even so, the measured

THz electric field distribution (uncorrected for either of these effects) has a FWHM of  $\sim 500 \mu\text{m}$  (see Fig. 7). This corresponds to approximately  $\lambda/2$ , using the peak-amplitude wavelength of the radiation reaching the detector. The spectrum of the detected THz field at the center of the waveguide is shown in the inset of Fig. 7(a).

## 5. EXTREME SUBWAVELENGTH CONFINEMENT USING TAPERED PPWGS

So far, we have only studied the transverse component ( $E_y$ ) of the electric field emerging from the waveguides. Surface

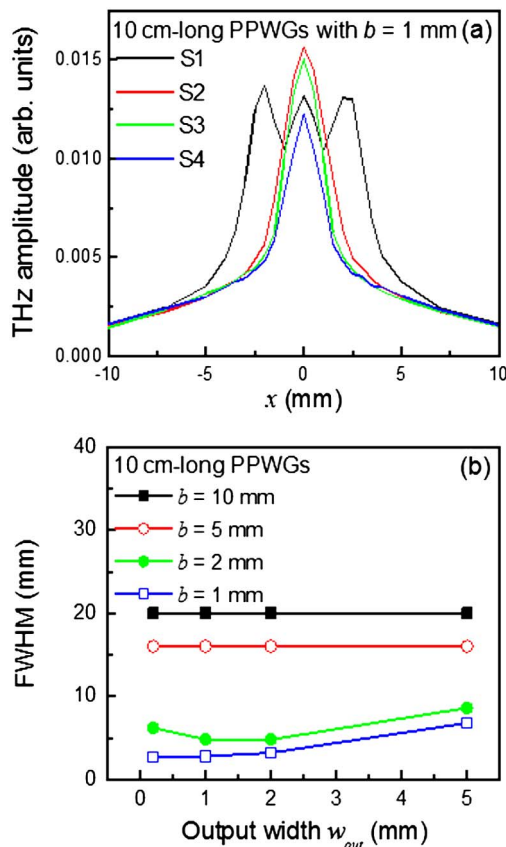


Fig. 5. (Color online) (a) One-dimensional  $x$ -axis scans (centered along the  $y$  direction) of the THz field (peak-to-peak amplitude) from the 10 cm long tapered PPWGs (S1–S4) with  $b = 1$  mm. (b) The dependence of the FWHM of the  $x$ -axis scans on the output width along the  $x$  axis, at plate separations of  $b = 10, 5, 2,$  and  $1$  mm for S1–S4.

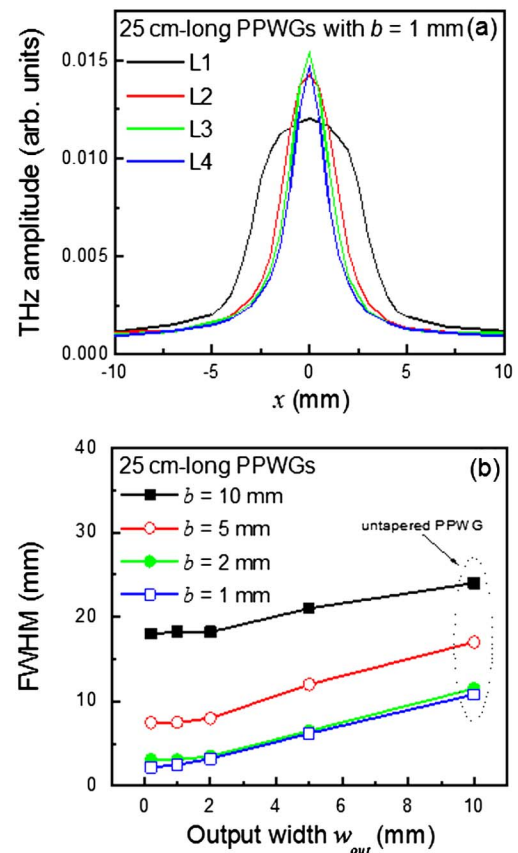


Fig. 6. (Color online) (a) One-dimensional  $x$ -axis scans (centered along the  $y$  direction) of the THz field (peak-to-peak amplitude) from the 25 cm long tapered PPWGs (L1–L4) with  $b = 1$  mm. (b) The dependence of the FWHM of the  $x$ -axis scans on the output width along the  $x$  axis, at plate separations of  $b = 10, 5, 2,$  and  $1$  mm for L1–L4 and for the untapered waveguide.

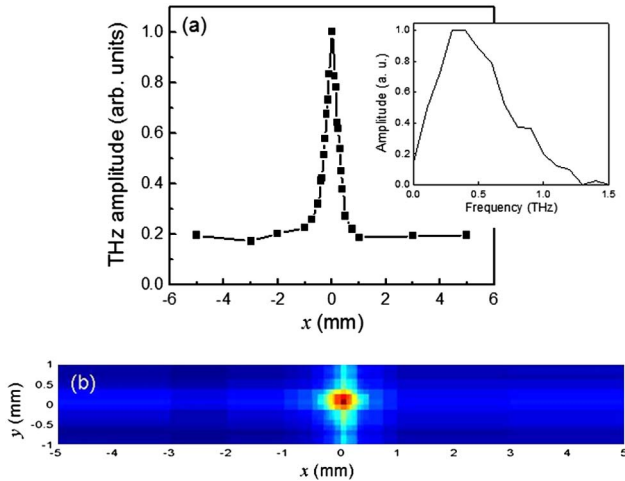


Fig. 7. (Color online) (a) THz output field (peak-to-peak amplitude) distribution along the horizontal axis at  $y = 0$  mm, localized to roughly  $\lambda/2$  in dimension from the tapered PPWG M1 with  $w_{\text{out}} = 120 \mu\text{m}$  and  $b_{\text{out}} = 100 \mu\text{m}$ . The inset gives a typical detected spectrum. (b) 2D field profile (peak-to-peak amplitude) measured at the output of the waveguide.

plasmon waves propagating along a metal/dielectric interface also have a  $z$  component (pointing along the propagation direction). This component also decays exponentially away from the metal surface and is much smaller than the  $y$  component, estimated from  $E_z/E_y = -\sqrt{\epsilon_{\text{air}}/\epsilon_{\text{metal}}} \sim 10^{-5}$ , because  $\epsilon_{\text{metal}}$  (equal to  $-3.7 \times 10^4 + i7.1 \times 10^5$  at 1 THz) is much larger than  $\epsilon_{\text{air}}$ . We are unable to measure  $E_z$  using the previously described detection method [illustrated in Figs. 1(a) and 1(b)] due to the polarization sensitivity of the receiver. Furthermore, a millimeter-scale spatial resolution is inadequate to study the field distribution at the output of tapered PPWGs with submillimeter dimensions.

In order to overcome these limitations, we use a different measurement technique to detect  $E_z$  in the vicinity of the output end of the tapered waveguides. This technique, illustrated in Fig. 1(c), is known as scattering-probe imaging [42]. Here, a sharp tungsten probe needle is mounted on a piezoelectric actuator, vibrating along the  $z$  direction with an amplitude of  $20 \mu\text{m}$  and a frequency of 160 Hz. We use needles with point diameters varying from 20 to  $2 \mu\text{m}$ , depending on the size of the output width  $w_{\text{out}}$ . The electric field emerging from the output of the waveguide is scattered by the probe needle and detected in the far field by the THz receiver. The detected signal is sensitive to the near-field component parallel to the vibration direction, which is  $E_z$  in this case. The receiver signal is sent to a lock-in amplifier, which is referenced to the vibration frequency. This detection technique is similar to apertureless near-field microscopy, applied to the case of free-space propagating fields. The spatial resolution is limited by the size of the probe tip, and can therefore be much smaller than the free-space wavelength [27,42].

We initially use a 25 cm long tapered PPWG (waveguide M2) with the output width  $w_{\text{out}}$  polished down to  $\sim 100 \mu\text{m}$ . The plate separation is adjusted to taper from  $b_{\text{in}} = 1$  mm to  $b_{\text{out}} \sim 110 \mu\text{m}$ . By scanning the probe needle in the  $x$  direction, with the tip held  $\sim 10 \mu\text{m}$  away from the waveguide output facet, we measure the field distribution along the  $x$  direction. These results are shown in Fig. 8(a). The FWHM of the field distribution is approximately  $108 \mu\text{m}$ , which is roughly equal

to  $w_{\text{out}}$ . It corresponds to approximately  $\lambda/24$ , given the peak-amplitude wavelength  $\lambda \approx 2.6$  mm. Figure 8(b) is the result of a scan along the propagation ( $z$ ) direction, fit to a  $1/z$  dependence given by the solid red curve. The excellent agreement with theory suggests that the  $z$  component of the field mimics the resultant field of an oscillating dipole. Figure 9(a) shows a 2D map in the  $x$ - $z$  plane near the top plate, again indicating the high lateral confinement.

Other interesting results are noted when scanning the probe needle along the  $y$  direction, across the air gap. We observe opposite polarities for  $E_z$  near the two metal plates, as indicated by the sign flip at the waveguide center ( $y = 0$ ) in Fig. 8(c). The 2D maps of the  $y$ - $z$  plane and the  $x$ - $y$  plane in Figs. 9(b) and 9(c) both illustrate this antisymmetric field distribution. This result is in agreement with previous numerical simulations [8,10,11,15,21,26], which have predicted that surface plasmons with antisymmetric charge distributions are long-range plasmonic modes with even  $H_x$  and  $E_y$  field components and an odd  $E_z$  component. These so-called

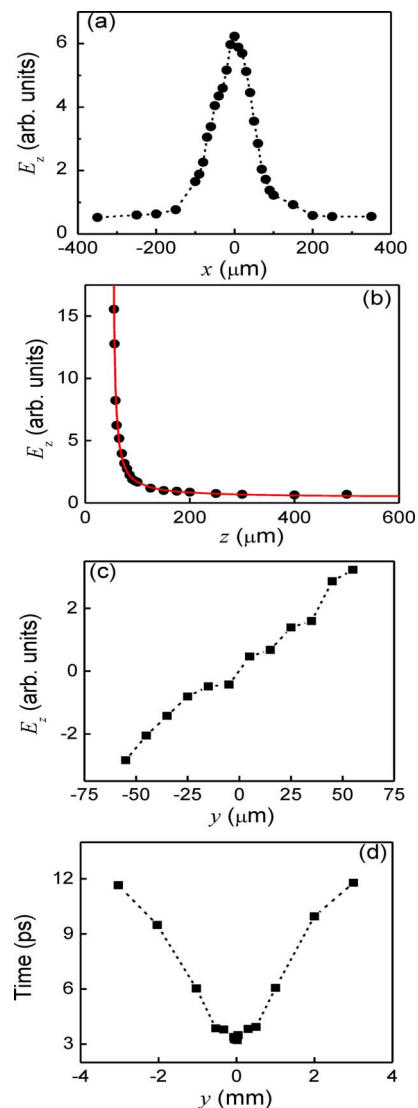


Fig. 8. (Color online) (a) 1D  $x$ -axis scan, (b) 1D  $z$ -axis scan fit to a theoretical (solid red) curve, and (c) 1D  $y$ -axis scan, all measured (peak-to-peak amplitude) at the end of the 25 cm long tapered PPWG M2 with  $w_{\text{out}} = 100 \mu\text{m}$  and  $b_{\text{out}} = 110 \mu\text{m}$ . (d) The time delay of  $E_z$  is shown along the  $y$  axis at  $x = 0$  mm.

symmetric modes have no cutoff and can propagate in an extremely small guiding area. However, surface plasmons with symmetric charge distributions become evanescent below a cutoff frequency, for a given plate separation.

In contrast to the highly confined  $E_z$  component in  $x$ - $z$  plane, the 2D map in  $y$ - $z$  plane at  $x = 0$  in Fig. 9(c) shows strong divergence in the  $y$  direction near  $z = 0$ . We can understand this extended field distribution by extracting the time delay at which the peak of the THz signal appears, as a function of position along the  $y$  axis. These time delays are plotted in Fig. 8(d). Note that the  $y$ -axis scale in this plot is much larger than the plate separation. The nearly linear increase in time delay with increasing distance from the waveguide center (at  $y = 0$ ) clarifies the nature of these diffracted fields. They are propagating waves, still closely associated with the metal surfaces, propagating away from the waveguide output aperture along the output facet.

Because each pixel in our 2D map is a time-domain waveform, we can assemble this data set in the form of an animation, and this is presented in Fig. 10 (Media 1). In this movie, we show the evolution of the  $E_z$  field amplitude in the  $x$ - $y$  plane (near the output facet) as time increases. We can clearly see the THz spot emerge at the output port of the waveguide and then propagate along both the positive and negative  $y$  axes, as the plasmon waves travel along the metal surfaces that comprise the output facet of the waveguide. This phenomenon results from the subwavelength aperture size of the output facet, and is similar to the highly diffracted output beam from terahertz quantum-cascade lasers using metal/metal waveguides [43,44]. This suggests that when using a tapered PPWG as a subwavelength probe tip, the distance from the output facet to the sample will be critical for achieving high spatial resolution [24]. This also suggests that engineering the nature (geometry) of the output facet may be useful for

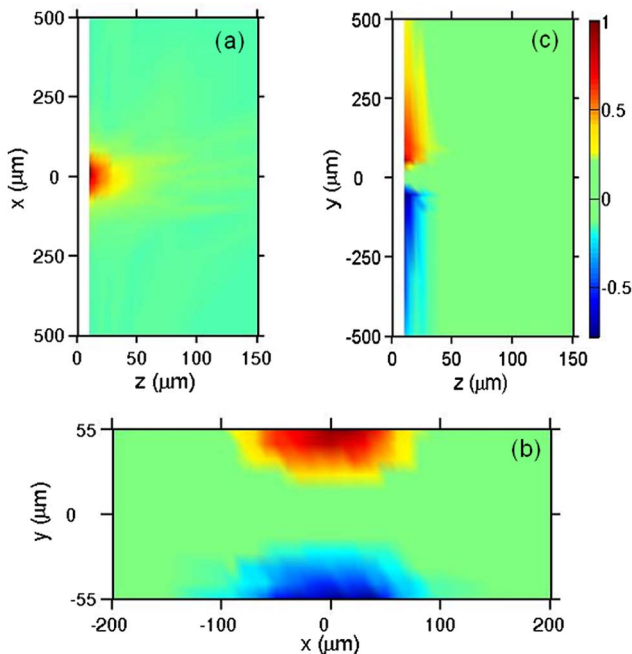


Fig. 9. (Color online) Two-dimensional field map (peak-to-peak amplitude) in the (a)  $x$ - $z$ , (b)  $x$ - $y$ , and (c)  $y$ - $z$  planes of  $E_z$  at the end of the tapered PPWG M2.

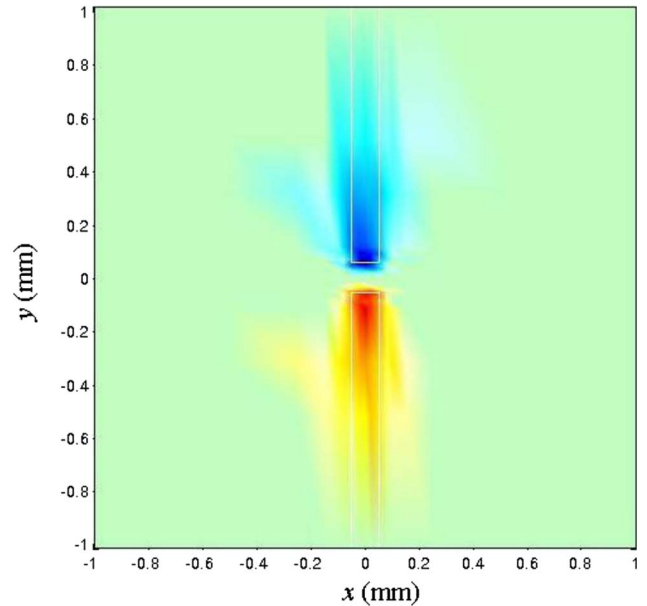


Fig. 10. (Color online) Evolution of the electric field ( $E_z$ ) map (Media 1) in the  $x$ - $y$  plane at the output facet of the waveguide. The thin white line shows the contours of two metal plates. The horizontal direction is the  $x$  axis, and the vertical direction is the  $y$  axis.

improving the coupling of radiation to the far field [45], similar to what can be achieved by attaching a silicon lens.

Because the symmetric plasmonic mode is the long-range mode with no cutoff, we can manipulate both  $w_{\text{out}}$  and  $b_{\text{out}}$  to realize extreme subwavelength confinement of the broadband THz field. Figure 11 shows 1D scans along the  $x$  axis, for three different tapered PPWGs (M2, M3, and M4) with decreasing plate separation and plate width. The measured FWHM of the output THz beam from each waveguide is roughly equal to  $w_{\text{out}}$ . The narrowest confinement along the  $x$  direction is about  $\lambda/260$  (using the peak-amplitude wavelength corresponding to 0.115 THz), corresponding to a mode area of only  $2.6 \times 10^{-5}$  of  $\lambda^2$ , with a plate separation of  $18 \mu\text{m}$  in the  $y$  direction. This demonstrates that the THz field can be strongly

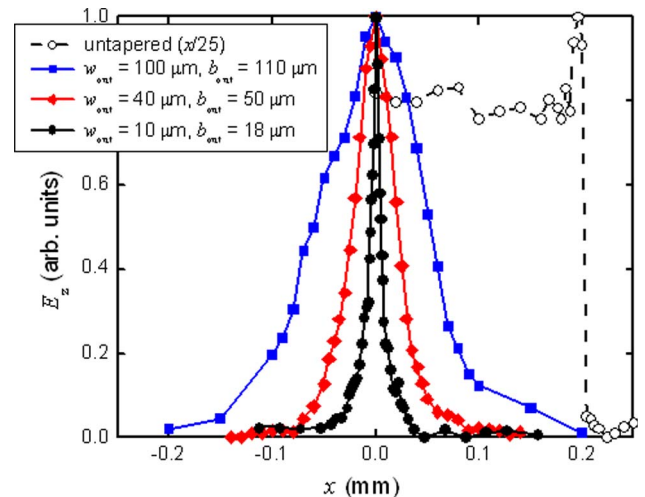


Fig. 11. (Color online) Line scans (peak-to-peak amplitude) along the  $x$  axis at the output of tapered waveguides M2-M4, with decreasing values of  $w_{\text{out}}$  and  $b_{\text{out}}$ . The dashed line shows the line scan at the output of an untapered 1 cm wide PPWG with an equivalent measurement, with the  $x$  axis scaled down by 25. Here, the plate separation is tapered similar to M4.

squeezed to a subwavelength spot in both lateral dimensions even when there is no confining material along the  $x$  direction.

The dashed line in Fig. 11 shows the 1D field profile at the output of an untapered 1 cm wide PPWG using an equivalent measurement technique. For comparison, the  $x$  axis is scaled down by a factor of 25. We note a sharp jump of the THz signal amplitude around the edge of the metal plate. This edge enhancement is consistent with the edge effect of  $E_y$  seen in Fig. 3(d). Figure 12(a) shows the time-domain waveforms at the output of an untapered 1 cm wide PPWG (black and gray curves), compared with an equivalent measurement on a tapered PPWG (M4) (red and blue curves). The similar temporal structure of these four waveforms indicates that the waveguide taper has minimal effect on the shape of the time-domain signal. The polarity flip mentioned above (see Fig. 9) is also evident in the comparisons of the time-domain waveforms measured at the upper (red and black curves) and lower (blue and gray curves) plate surfaces. The comparison of the corresponding amplitude spectra for the tapered and unta-

pered cases is presented in Fig. 12(b). The nearly identical spectra indicate that there is no significant bandwidth limitation and no frequency cutoff imposed by the tapering, even though the output radiation spot size is hundreds of times smaller than the wavelength. The tapered PPWG provides extreme subwavelength confinement along with broad spectral bandwidths.

## 6. CONCLUSION

In summary, we have experimentally characterized the THz near-field output of PPWGs and demonstrated how to achieve extreme subwavelength 2D confinement using these devices. The scale of the 2D confinement is limited by the plate width and plate separation (above the skin-depth limitation). The fact that the detected longitudinal field ( $E_z$ ) shows an anti-symmetric field distribution confirms that the propagating mode in the tapered subwavelength structure is the long-range SPP mode. These results support the use of tapered PPWGs for applications in THz spectroscopy, sensing, and imaging with extreme subwavelength spatial resolution.

## REFERENCES

1. M. Quinten, A. Leitner, J. R. Krenn, and F. R. Aussenegg, "Electromagnetic energy transport via linear chains of silver nanoparticles," *Opt. Lett.* **23**, 1331–1333 (1998).
2. S. A. Maier, M. L. Brongersma, and H. A. Atwater, "Electromagnetic energy transport along arrays of closely spaced metal rods as an analogue to plasmonic devices," *Appl. Phys. Lett.* **78**, 16–18 (2001).
3. K. Tanaka and M. Tanaka, "Simulations of nanometric optical circuits based on surface plasmon polariton gap waveguide," *Appl. Phys. Lett.* **82**, 1158–1160 (2003).
4. K. Tanaka, G. W. Burr, T. Grosjean, T. Maletzky, and U. C. Fischer, "Superfocussing in a metal-coated tetrahedral tip by dimensional reduction of surface-to edge-plasmon modes," *Ann. Phys. B* **93**, 257–266 (2008).
5. M. I. Stockman, "Nanofocusing of optical energy in tapered plasmonic waveguides," *Phys. Rev. Lett.* **93**, 137404 (2004).
6. R. Zia, M. D. Selker, P. B. Catrysse, and M. L. Brongersma, "Geometries and materials for subwavelength surface plasmon modes," *J. Opt. Soc. Am. A* **21**, 2442–2446 (2004).
7. S. I. Bozhevolnyi, V. S. Volkov, E. Devaux, and T. W. Ebbesen, "Channel plasmon-polariton guiding by subwavelength metal grooves," *Phys. Rev. Lett.* **95**, 046802 (2005).
8. D. K. Gramotnev, "Adiabatic nanofocusing of plasmons by sharp metallic grooves: geometrical optics approach," *J. Appl. Phys.* **98**, 104302 (2005).
9. L. Liu, Z. Han, and S. He, "Novel surface plasmon waveguide for high integration," *Opt. Express* **13**, 6645–6650 (2005).
10. D. F. P. Pile, T. Ogawa, D. K. Gramotnev, Y. Matsuzaki, K. C. Vernon, K. Yamaguchi, T. Okamoto, M. Haraguchi, and M. Fukui, "Two-dimensionally localized modes of a nanoscale gap plasmon waveguide," *Appl. Phys. Lett.* **87**, 261114 (2005).
11. D. F. P. Pile, D. K. Gramotnev, M. Haraguchi, T. Okamoto, and M. Fukui, "Numerical analysis of coupled wedge plasmons in a structure of two metal wedges separated by a gap," *J. Appl. Phys.* **100**, 013101 (2006).
12. D. F. P. Pile and D. K. Gramotnev, "Adiabatic and nonadiabatic nanofocusing of plasmons by tapered gap plasmon waveguides," *Appl. Phys. Lett.* **89**, 041111 (2006).
13. G. Veronis and S. Fan, "Guided subwavelength plasmonic mode supported by a slot in a thin metal film," *Opt. Lett.* **30**, 3359–3361 (2005).
14. G. Veronis and S. Fan, "Modes of subwavelength plasmonic slot waveguides," *J. Lightwave Technol.* **25**, 2511–2521 (2007).
15. J. A. Dionne, L. A. Sweatlock, and H. A. Atwater, "Plasmon slot waveguides: towards chip-scale propagation with subwavelength-scale localization," *Phys. Rev. B* **73**, 035407 (2006).

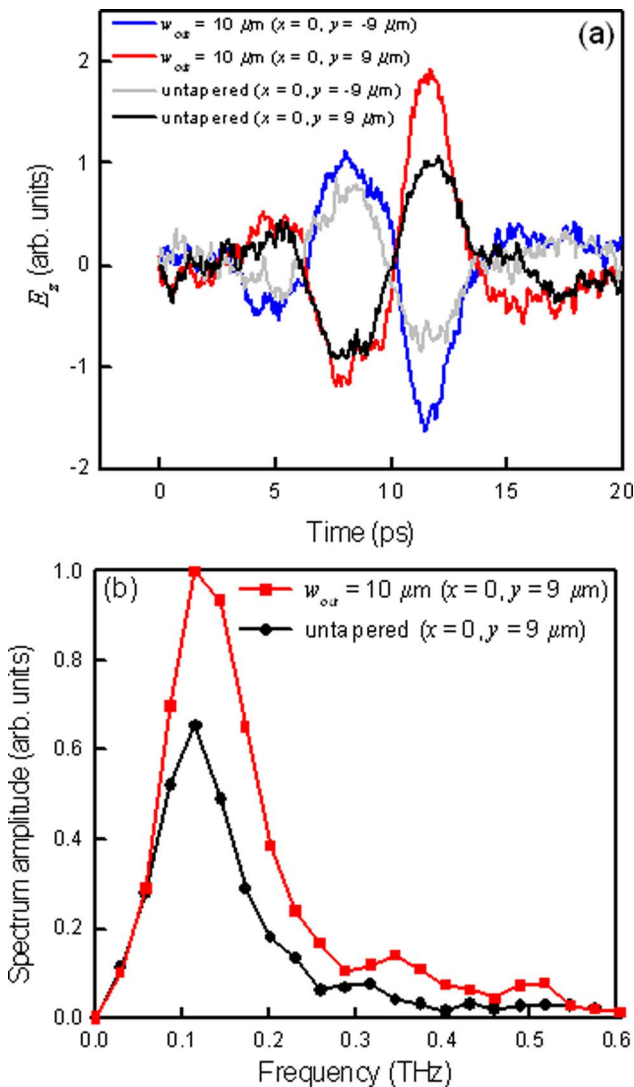


Fig. 12. (Color online) (a) Waveforms measured at the output facet of the tapered PPWG M4 and an untapered 1 cm wide waveguide. These are measured using identical methods so that the waveforms can be compared. (b) The amplitude spectra show no bandwidth restrictions even though  $w_{out}$  is much smaller than the free-space wavelength in the tapered case.

16. P. Ginzburg, D. Arbel, and M. Orenstein, "Gap plasmon polariton structure for very efficient microscale-to-nanoscale interfacing," *Opt. Lett.* **31**, 3288–3290 (2006).
17. E. Verhagen, L. Kuipers, and A. Polman, "Enhanced nonlinear optical effects with a tapered plasmonic waveguide," *Nano Lett.* **7**, 334–337 (2007).
18. E. Verhagen, A. Polman, and L. Kuipers, "Nanofocusing in laterally tapered plasmonic waveguides," *Opt. Express* **16**, 45–57 (2008).
19. E. Verhagen, M. Spasenovic, A. Polman, and L. Kuipers, "Nanowire plasmon excitation by adiabatic mode transformation," *Phys. Rev. Lett.* **102**, 203904 (2009).
20. K. C. Vernon, D. K. Gramotnev, and D. F. P. Pile, "Adiabatic nanofocusing of plasmons by a sharp metal wedge on a dielectric substrate," *J. Appl. Phys.* **101**, 104312 (2007).
21. J. Wuenschell and H. K. Kim, "Excitation and propagation of surface plasmons in a metallic nanoslit structure," *IEEE Trans. Nano.* **7**, 229–236 (2008).
22. R. Yang, M. A. G. Abushagur, and Z. Lu, "Efficiently squeezing near infrared light into a 21 nm-by-24 nm nanospot," *Opt. Express* **16**, 20142–20148 (2008).
23. H. T. Chen, R. Kersting, and G. C. Cho, "Terahertz imaging with nanometer resolution," *Appl. Phys. Lett.* **83**, 3009–3011 (2003).
24. N. Klein, P. Lahl, and U. Poppe, "A metal-dielectric antenna for terahertz near-field imaging," *J. Appl. Phys.* **98**, 014910 (2005).
25. M. Wächter, M. Nagel, and H. Kurz, "Metallic slit waveguide for dispersion-free low-loss terahertz signal transmission," *Appl. Phys. Lett.* **90**, 061111 (2007).
26. A. Rusina, M. Durach, K. A. Nelson, and M. I. Stockman, "Nano-concentration of terahertz radiation in plasmonic waveguides," *Opt. Express* **16**, 18576–18589 (2008).
27. V. Astley, R. Mendis, and D. M. Mittleman, "Characterization of terahertz field confinement at the end of a tapered metal wire waveguide," *Appl. Phys. Lett.* **95**, 031104 (2009).
28. X. Lu and W. Zhang, "Terahertz localized plasmonic properties of subwavelength ring and coaxial geometries," *Appl. Phys. Lett.* **94**, 181106 (2009).
29. A. Ishikawa, S. Zhang, D. A. Genov, G. Bartal, and X. Zhang, "Deep subwavelength terahertz waveguides using gap magnetic plasmon," *Phys. Rev. Lett.* **102**, 043904 (2009).
30. H. Zhan, R. Mendis, and D. M. Mittleman, "Superfocusing terahertz waves below  $\lambda/250$  using plasmonic parallel-plate waveguides," *Opt. Express* **18**, 9643–9650 (2010).
31. R. Mendis and D. Grischkowsky, "Undistorted guided-wave propagation of subpicosecond terahertz pulses," *Opt. Lett.* **26**, 846–848 (2001).
32. R. Mendis and D. M. Mittleman, "An investigation of the lowest-order transverse-electric ( $TE_1$ ) mode of the parallel-plate waveguide for THz pulse applications," *J. Opt. Soc. Am. B* **26**, A6–A13 (2009).
33. D. Mittleman, *Sensing with Terahertz Radiation*, Springer Series in Optical Sciences (Springer-Verlag, 2002).
34. R. Mendis and D. Grischkowsky, "THz interconnect with low loss and low group velocity dispersion," *IEEE Microwave & Wireless Comp. Lett.* **11**, 444–446 (2001).
35. J. R. Wait, "On the theory of shielded surface waves," *IEEE Trans. Microw. Theory Tech.* **15**, 410–414 (1967).
36. H. M. Barlow, "New features of wave propagation not subject to cutoff between two parallel guiding surfaces," *Proc. IEEE* **114**, 421–427 (1967).
37. H. M. Barlow, "High-frequency wave propagation between parallel surfaces very close together," *J. Phys. D: Appl. Phys.* **6**, 929–935 (1973).
38. M. Gong, T.-I. Jeon, and D. Grischkowsky, "THz surface wave collapse on coated metal surfaces," *Opt. Express* **17**, 17088–17101 (2009).
39. T.-I. Jeon and D. Grischkowsky, "THz Zenneck surface wave (THz surface plasmon) propagation on a metal sheet," *Appl. Phys. Lett.* **88**, 061113 (2006).
40. V. R. Almeida, Q. Xu, C. A. Barrios, and M. Lipson, "Guiding and confining light in void nanostructure," *Opt. Lett.* **29**, 1209–1211 (2004).
41. Q. Xu, V. R. Almeida, R. R. Panepucci, and M. Lipson, "Experimental demonstration of guiding and confining light in nanometer-size low-refractive-index material," *Opt. Lett.* **29**, 1626–1628 (2004).
42. V. Astley, H. Zhan, R. Mendis, and D. M. Mittleman, "A study of background signals in terahertz apertureless near-field microscopy and their use for scattering-probe imaging," *J. Appl. Phys.* **105**, 113117 (2009).
43. B. Williams, "Terahertz quantum-cascade lasers," *Nat. Photon.* **1**, 517–525 (2007).
44. S. Kohen, B. Williams, and Q. Hu, "Electromagnetic modeling of terahertz quantum cascade laser waveguides and resonators," *J. Appl. Phys.* **97**, 053106 (2005).
45. N. Yu, J. Fan, Q. J. Wang, C. Pflügl, L. Diehl, T. Edamura, M. Yamamishi, H. Kan, and F. Capasso, "Small-divergence semiconductor laser by plasmonic collimation," *Nat. Photon.* **2**, 564–570 (2008).